Materials Today Nano 22 (2023) 100322

Contents lists available at ScienceDirect

Materials Today Nano

journal homepage: https://www.evise.com/profile/#/MTNANO/login

Cycle-stable Si-based composite anode for lithium-ion batteries enabled by the synergetic combination of mixed lithium phosphates and void-preserving F-doped carbon

Zhefei Sun [a, 1], Miao Li [a, 1], Zhiming Zheng [a, 1], Zhilin Chen [a], Hehe Zhang [a], Bensheng Xiao [a], Baihua Qu [d], Bing Jiang [c], Honggang Liao [b], Li Zhang [b], Meicheng Li [c], Qiaobao Zhang [a, *], Ming-Sheng Wang [a, **]

[a] State Key Laboratory of Physical Chemistry of Solid Surfaces, College of Materials, Xiamen University, Xiamen, 361005, China
[b] State Key Laboratory of Physical Chemistry of Solid Surfaces, College of Chemistry and Chemical Engineering, Xiamen University, Xiamen, Fujian, 361005, China
[c] State Key Laboratory of Alternate Electrical Power System with Renewable Energy Sources, School of New Energy, North China Electric Power University, Beijing, 102206, China
[d] College of Materials Science and Engineering, Chongqing University, Chongqing, 400044, China

ARTICLE INFO

Article history:
Received 6 January 2023
Received in revised form
22 February 2023
Accepted 26 February 2023
Available online 3 March 2023

Keywords:
Si-based anode materials
Lithium-ion batteries
In situ TEM observations
Electrochemical performance

ABSTRACT

Silicon-based materials have been considered as the promising anode candidates for next-generation high-energy-density lithium-ion batteries (LIBs). However, their widespread application is unfortunately restricted by severe volume variations during cycling and poor electronic conductivity. To overcome these challenges, we showcase an innovative design of dual core–shell structured Si-based nanocomposites working as anode for LIBs with boosted performance, where the Si nanoparticle core is tightly wrapped by a mixed lithium phosphate (Li_3PO_4/$Li_4P_2O_7$) shell and void-preserving F-doped carbon shell (denoted as Si@LPO@void@FC). For such novel structured composite, the inner L_3PO_4/$Li_4P_2O_7$ layer acting as artificial solid-electrolyte interphase (SEI) and the outer void-preserving F-doped C can effectively tolerate the volume changes while ensuring the stability of SEI layer, facilitate the Li^+ migration and electron transfer, and reinforce the structural stability during cycling. Consequently, the as-fabricated Si@LPO@void@FC anode exhibits a reversible capacity of 569 mAh/g after 500 cycles at 1 A/g, and an exceptional long-term cycling stability with 76% capacity retention over 1000 cycles at 4.0 A/g can be achieved. Additionally, the full cell assembled with Si@LPO@void@FC anode and $LiFePO_4$ cathode also demonstrates a good cycling performance with 117 mAh/g at 1 C for over 150 cycles with 92% capacity retention, suggesting the potentiality for practical application. Furthermore, the mechanisms of the enhanced structural stability of Si@LPO@void@FC anode are carefully elaborated by substantial *in situ*/*ex situ* microscopic techniques and electrochemical tests. It is expected that our findings in this work can provide guiding significance for improving the cycling performance of Si-based composite anodes toward high-performance LIBs.

1. Introduction

Owing to the conspicuous merits of extremely high theoretical capacity (3579 mAh/g), appropriate working potential (~0.4 V vs Li^+/Li) and abundant reserves, the silicon (Si) anode has been identified as a prime alternative to the commercial graphite anode for high-energy-density lithium-ion batteries (LIBs) [1,2]. Nevertheless, the Si anode is usually subjected to huge volume variations during cycling (~300%) [3], leading to the occurrence of cracking and pulverization of Si particles (>150 nm) [4] associated with uncontrolled growth of solid-electrolyte interface (SEI) [5], eventually, unsatisfied low Coulombic efficiency (CE) and fast capacity degradation are produced. To tackle this challenge, tremendous efforts have been devoted to prolong the lifespan of Si-based anodes [6–8]. For example, reducing the size of Si to nanoscale has been shown to mitigate its pulverization, and thus better cycling

* Corresponding author.
** Corresponding author.
E-mail addresses: zhangqiaobao@xmu.edu.cn (Q. Zhang), mswang@xmu.edu.cn (M.-S. Wang).
[1] These authors contributed equally to this work.

https://doi.org/10.1016/j.mtnano.2023.100322
2588-8420/

performance can be obtained [9–11]. However, the nanostructured Si with large specific surface area normally has more serious parasitic electrolyte decomposition reactions, giving rise to lower initial Coulomibic efficiency (ICE) [12]. Generally, it is believed that the addition of fluoroethylene carbonate (FEC) or vinylene carbonate (VC) in electrolyte is favorable for reducing the side reactions and constructing robust SEI on nanostructured Si with enhanced ICE and cycling stability [13]. Besides, the introduction of an artificial SEI layer into nanostructured Si can prevent the direct contact between Si and electrolyte, which has proven to be an effective strategy for alleviating the uncontrol growth of SEI to achieve better capacity retention [14–16].

By virtue of high ionic conductivity (4.5×10^{-7} S/cm), broad electrochemical window (0–4.7 V vs. Li^+/Li) [17] and excellent mechanical property (shear modules, 103.4 GPa) [18], lithium phosphate (Li_3PO_4) working as mechanically robust artificial SEI has been adopted as stable interfacial layers in Si or Li metallic anode [18–20]. Accordingly, the unfavorable reaction between electrodes and the electrolyte can be restrained and the Li^+ transport can be accelerated by the introduction of lithium phosphate. Additionally, the volume changes of Si anodes can be ameliorated during cycling [21], which makes great contributions to the enhanced rate and cycling performance. Moreover, it has been demonstrated that the mixed lithium phosphate of $Li_4P_2O_7/Li_3PO_4$ composites with good mechanical characteristics can exhibit higher ionic conductivity than that of single phase Li_3PO_4 and $Li_4P_2O_7$ [22], such composites are considered as appealing candidates for artificial SEI layer in high-capacity LIB anodes. Although the above-mentioned strategies can enhance the cycling performance of Si anode, its low intrinsic electronic conductivity is detrimental for the limited rate performance [7]. Surface coating of conductive carbonaceous materials with Si, forming Si/carbon composite has been demonstrated to boost the rate performance and cycling stability, which is attributed to the high electrical/ionic conductivities and high mechanical strength of carbonaceous materials [23,24]. However, only coated with conductive carbon layer can normally bear the huge volumetric stress induced by the repeated lithiation/delithiation of Si to a limited extent, resulting in the structural and interface instabilities and subsequent capacity fade during prolonged cycling [19]. In this regard, innovative strategies with the combination of artificial SEI design and surface carbon modification on Si-based anodes to simultaneously achieve the desirable high-rate capability and long-term cycling stability are thus particularly desirable. Notably, the research on the effects of integrating the $Li_4P_2O_7/Li_3PO_4$ coating with carbon decoration for Si anode to realize significant improvement in LIB performance has not been reported.

Herein, we showcase an innovative design of core–dual shell structured Si-based nanocomposite, in which the Si nanoparticle core is tightly wrapped by a dual of mixed lithium phosphate ($Li_3PO_4/Li_4P_2O_7$) and void-preserving F-doped carbon (denoted as Si@LPO@void@FC) working as anode for boosting LIB performance. In order to realize the enhanced performance, such ingenious design endows the resultant anode exhibiting the following attractive features: (i) the continues reaction between Si and electrolyte can be inhibited by the inner $Li_3PO_4/Li_4P_2O_7$ (LPO) layer and its huge volume change can be accommodated during cycling, as evidenced by *in situ* transmission electron microscopy (*in situ* TEM) observations; (ii) the *in situ* reserved voids between LPO and FC shell render space for further buffering the volume expansion of Si; (iii) the outer FC shell facilitate the electron/ion transportation and reinforce the structural stability during cycling. As a result, the as-prepared Si@LPO@void@FC anode shows superior lithium storage property in terms of high reversible capacity (569 mAh/g at 1 A/g after 500 cycles), exceptional long-term cycling performance (76% capacity retention, 1000 cycles at 4 A/g) and high-rate capability. Furthermore, the full cell fabricated by Si@LPO@void@FC anode and commercial $LiFePO_4$ cathode can deliver desirable durability (117 mAh/g after 150 cycles with 92% capacity retention). Additionally, the mechanisms of enhanced cycling performance are explicitly revealed through electrochemical tests, *in situ* TEM observation and *ex situ* microscopic techniques. It is expected that this work can provide important insights into constructing stable Si-based composite anodes for the realization of high-performance LIBs.

2. Results and discussion

The synthesis procedure of Si@LPO@void@FC is illustrated in Fig. 1a. First, the commercialized Si nanoparticles (Si NPs) and lithium acetate (LiAc) were added into deionized (DI) water under magnetic stirring. Second, the phytic acid (PA) and polytetrafluoroethylene (PTFE), acting as phosphorus source and carbon source, were added into the above solution. After freezing–drying, the obtained precursor powders were sintered under argon protection to form the Si@LPO@void@FC composite. For comparisons, three samples with different amount of commercial Si NPs (45 mg, 60 mg, and 90 mg) were fabricated and denoted as Si@LPO@void@FC_1, Si@LPO@void@FC_2 and Si@LPO@void@FC_3, respectively. Herein, the formation of voids can be ascribed to the different decomposition temperatures between LiAc, PA and PTFE [25–27]. Before carbonization process of PTFE, the decomposition of LiAc and PA was associated with the release of small molecular, and the formation of void-preserving structure was facilitated, which was similar to the previous reported works [28,29].

The detailed morphology and microstructure characteristics of as-prepared Si@LPO@void@FC were observed by scanning electron microscopy (SEM) and transmission electron microscopy (TEM). Compared with the pristine Si NPs (Fig. S1 a-c), the Si@LPO@void@FC were well covered by LPO and void-preserving FC with the decoration of small particles, as depicted in Fig. 1b and c. As shown in Fig. 1d, it is evident that there are several reserved voids in Si@LPO@void@FC, indicating the feasibility of constructing void-preserving structure by utilizing the different decomposition temperature of precursor. The diffraction spots belonging to Li_3PO_4, $Li_4P_2O_7$ and the diffraction rings corresponding to Si can be detected in the selected area electron diffraction (SAED) patterns of Si@LPO@void@FC (Fig. 1e), respectively. The distribution of Si, Li_3PO_4 and $Li_4P_2O_7$ can be further confirmed by high-resolution TEM (HRTEM), the relevant lattice fringes in Fig. 1f can be determined as 0.379, 0.314 and 0.318 nm (Fig. 1f_1, 1f_2 and 1f_3), corresponding to the lattice spacing of Li_3PO_4, Si and $Li_4P_2O_7$, respectively. These experimental results demonstrates that the Si NPs are well wrapped by the mixture of Li_3PO_4 and $Li_4P_2O_7$. Meanwhile, the lattice fringes of anchored particles on FC as marked in Fig. 1g with a spacing of 0.264 nm and 0.398 nm can be indexed to the (220) and (120) planes of Li_3PO_4 (Fig. 1g_1, g_2), which are consistent with the FFT patterns of anchored nanoparticles (Fig. S2). Furthermore, in order to demonstrate the generality of this method to form this novel structure, we replace LiAc with CH_3COONa (NaAc) as precursor, which possesses relative low decomposition temperature (~324 °C), and other experimental conditions were controlled as the same. Accordingly, voids can also be found in the product, as shown in Fig. S3a. This result suggests that other acetate materials could also be used for generating the voids. However, it should be noted that the thermal stability of carbon source is crucial to introduce voids. When polyvinylidene fluoride (PVDF) as carbon source is employed, which has lower pyrolyzing temperature (~316 °C) than PTFE (~415 °C), no void can be observed in the product, as shown in Fig. S3b.

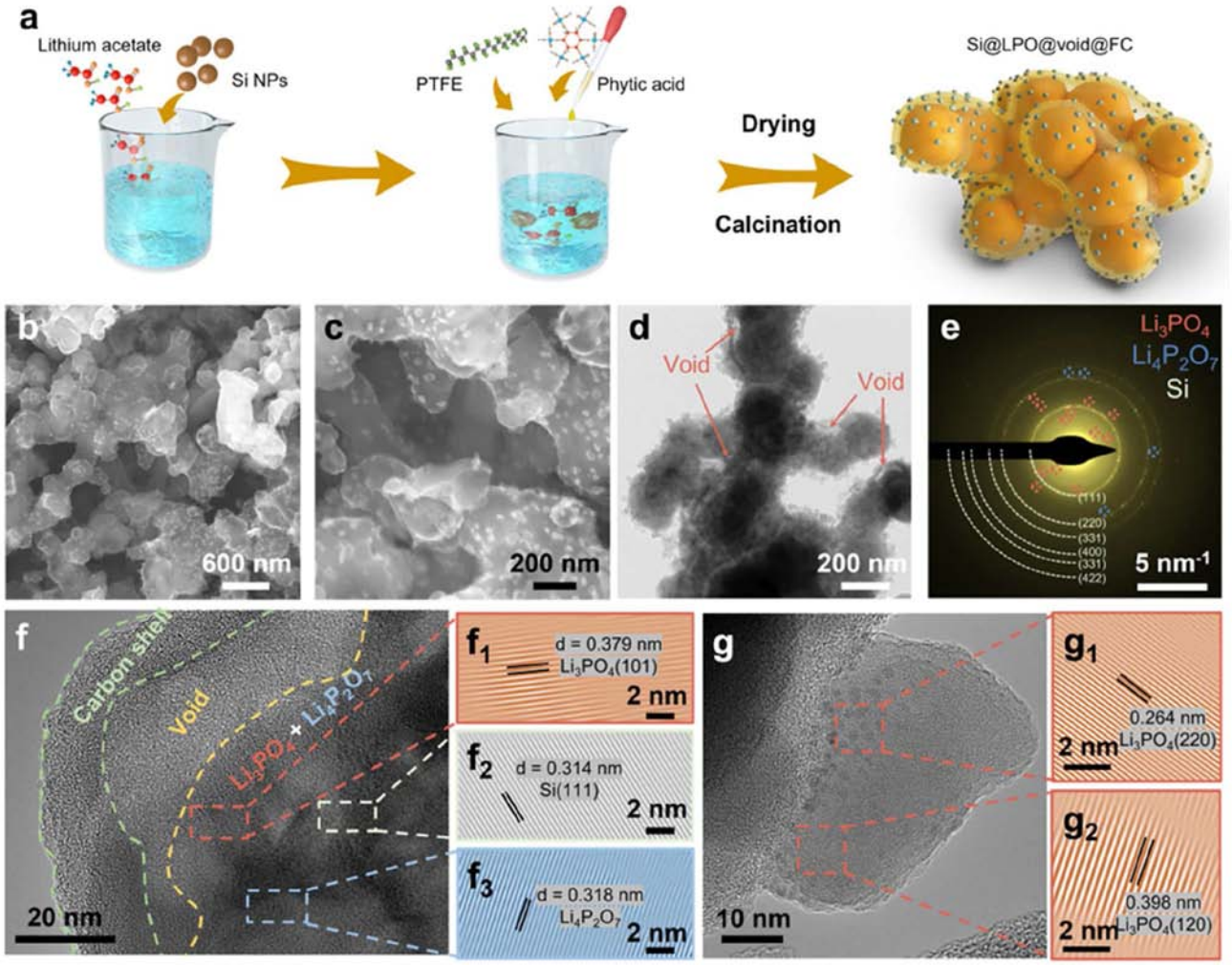

Fig. 1. (a) Schematic diagram of the fabrication process of Si@LPO@void@FC_2 composite. (b, c) SEM images, (d) TEM image, (e) SAED pattern of as-prepared Si@LPO@void@FC_2 sample. (f) HRTEM image of the edge region of sample, (f_1, f_2, f_3 are the inverse FFT images of selected area). (g) HRTEM image of anchored nanoparticles (g_1, g_2 are the inverse FFT images of selected area).

To further understand the phase constituents of Si@LPO@-void@FC, X-Ray diffraction (XRD) measurement was conducted, as shown in Fig. 2a. Diffraction peaks belonging to Li_3PO_4 and $Li_4P_2O_7$ can be detected in the XRD patterns, which are in good agreement with the TEM analysis. Moreover, three strong diffraction peaks located at 28.4°, 47.3° and 56.1° can be assigned to the (111), (220) and (311) facets of Si, respectively. The LPO in sample is most likely originated from the reaction between LiAc and PA, since Li_3PO_4 and $Li_4P_2O_7$ phases can be obtained when directly thermal treated LiAc-PA mixture (Fig. S4). Furthermore, the chemical compositions of Si@LPO@void@FC_2 were investigated by X-ray photoelectron spectroscopy (XPS) measurements. As shown in Fig. 2b, the XPS full spectrum reveals the presence of F, O, C, P and Si elements in the sample. The high-resolution spectra of P 2p (Fig. 2c) exhibits two strong characteristic peaks at 134.2 and 135.1 eV, respectively, which can be assigned to P—O bond that derived from Li_3PO_4 and $Li_4P_2O_7$ [30—32]. Besides, a strong peak located at 531.9 eV in the high-resolution spectra of O 1s (Fig. 2d) can be assigned as the P—O bond as well [32]. Another peak in the O 1s spectra which located at 533.7 eV can be ascribed to Si—O bond, consistent with the high-resolution spectra of Si 2p (Fig. S5a). It should be noted that the signal of Si—O is probably derived from the naturally formed SiO_2 on the surface of Si NPs, which is commonly observed in reported results of Si anodes [33,34]. For the C 1s spectra, as shown in Fig. 2e, the peak at 284.8, 285.3, 287.4 and 289.6 eV can be assigned to C—C/C=C, C—O, C—F and O=C—O, respectively [35,36]. Moreover, in the F 1s spectra (Fig. S5b), the peak at 688.1 eV also confirmed the existence of C—F configuration [35—37]. Additionally, the signal of Li 1s can be detected due to the formation of LPO layer (Fig. S5c). Thermo-gravimetric analysis (TGA) was further applied to clarify the content of FC in Si@LPO@void@FC, as shown in Fig. 2f. The mass fraction of FC is calculated to be 14.88 wt %. The Raman spectrum of Si@LPO@void@FC exhibits strong signal of Si, and the D band (~1346 cm^{-1}) and G band (~1586 cm^{-1}) representing the vibration of disordered carbon and graphitic carbon are clearly observed. The ratio of I_D/I_G is determined as 0.986, indicating the high graphitic degree of carbon shell in the sample. In addition, high-angle annular dark-field (HAADF) scanning TEM (STEM) and elemental mappings of Si@LPO@void@FC_2 give the evidences for the existence of the Si, C, P, O and F in as-prepared sample (Fig. 2g). The signal of P (Fig. 2g_1), O (Fig. 2g_2) and C (Fig. 2g_4) are uniformly distributed on the surface of Si NPs (Fig. 2g_3), suggesting that the Si NPs are well wrapped by $Li_3PO_4/Li_4P_2O_7$ and FC. According to energy dispersive spectra (EDS) of Si@LPO@void@FC_2 (Fig. 2h), the mass fractions of Si, C, P, O and F atoms are determined as 39.46%, 20.17%, 2.02%, 37.53%, 0.83%, respectively. Besides these elements, the signal of Cu

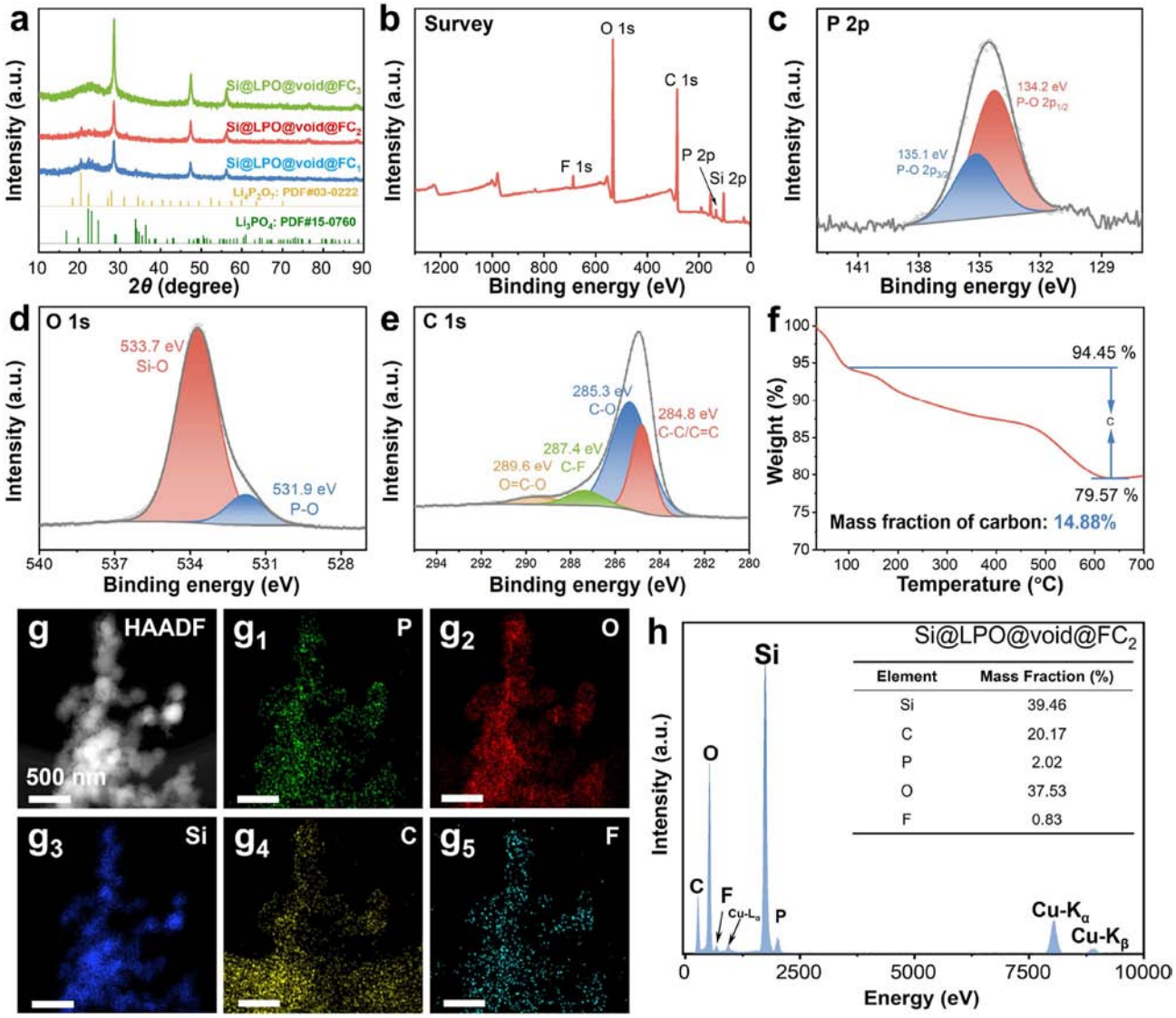

Fig. 2. (a) XRD patterns of Si@LPO@void@FC composites. (b) Full-scale XPS spectrum, high resolution XPS spectra of (c) P 2p, (d) O 1s and (e) C 1s, respectively. (f) TG pattern of Si@LPO@void@FC_2. (g) HADDF image and the corresponding elemental mappings of (g_1) P, (g_2) O, (g_3) Si, (g_4) C and (g_5) F. (h) EDS analysis of Si@LPO@void@FC_2 and the corresponding elemental contents.

was also detected in EDS, which is originated from Cu grids. In addition, the EDS results of Si@LPO@void@FC_1 and Si@LPO@void@FC_3 are acquired as well (Fig. S7a-b) and the mass ratios of Si and P for the three samples are presented in Table S1.

To evaluate the effects of LPO and void-preserving FC on the electrochemical performance of Si-based anodes, the related electrochemical performance testing was carried out. For comparison, as-obtained commercial Si anode was tested as well. First, the cyclic voltammetry (CV) tests were conducted to explore the reaction mechanism of Si@LPO@void@FC_2 anode (Fig. 3a). Two cathodic peaks located at 0.18 V and near 0.005 V can be detected, which is related to the alloying process of Si. As for the delithiation process, two anodic peaks at 0.38 and 0.52 V can be clearly seen, corresponding to the phase transformation process of Li_xSi. These results are in good agreement with the previous work [38]. Apart from the peaks as mentioned above, other cathodic and anodic peaks can be neglected, suggesting that the LPO layer cannot participate the reactions during cycling.

Fig. 3b presents the galvanostatic charge-discharge profiles of the Si@LPO@void@FC_2 electrode at 1 A/g. During the first cycle, the initial discharge and charge capacities of the electrode reach 936.1 and 767.2 mAh/g, respectively, corresponding to an ICE of 81.9%. The capacity loss in the first cycle is highly related to the electrolyte decomposition and the formation of SEI layer. During the second cycle, a relatively stable SEI is generated and the CE is rapidly increased to 89.1% with the discharge/charge capacities of 806.3 and 718.1 mAh/g. Subsequently, the charge-discharge profiles remain stable, suggesting that a good cycling stability can be obtained. Fig. 3c shows the cycling performance of three as-prepared Si@LPO@void@FC anodes at 1 A/g. Due to the protection of constructed artificial SEI of LPO and FC, all the three electrodes present superior cycling performance to that of bare Si anode (Fig. S8 a-c). The cycling stability and reversible capacity of Si@LPO@void@FC anodes are found to strongly dependent on the content of LPO. Although the Si@LPO@void@FC_3 presents higher initial discharge capacity (920.7 mAh/g) than that of Si@LPO@void@FC_1 (424.6 mAh/g) and Si@LPO@void@FC_2 (605.5 mAh/g), the reversible capacity faded much faster, only 70% capacity retention is retained after 500 cycles at 1 A/g. In contrast, the Si@LPO@void@FC_1 and Si@LPO@void@FC_2 anodes exhibit superior cycling stability with the capacity

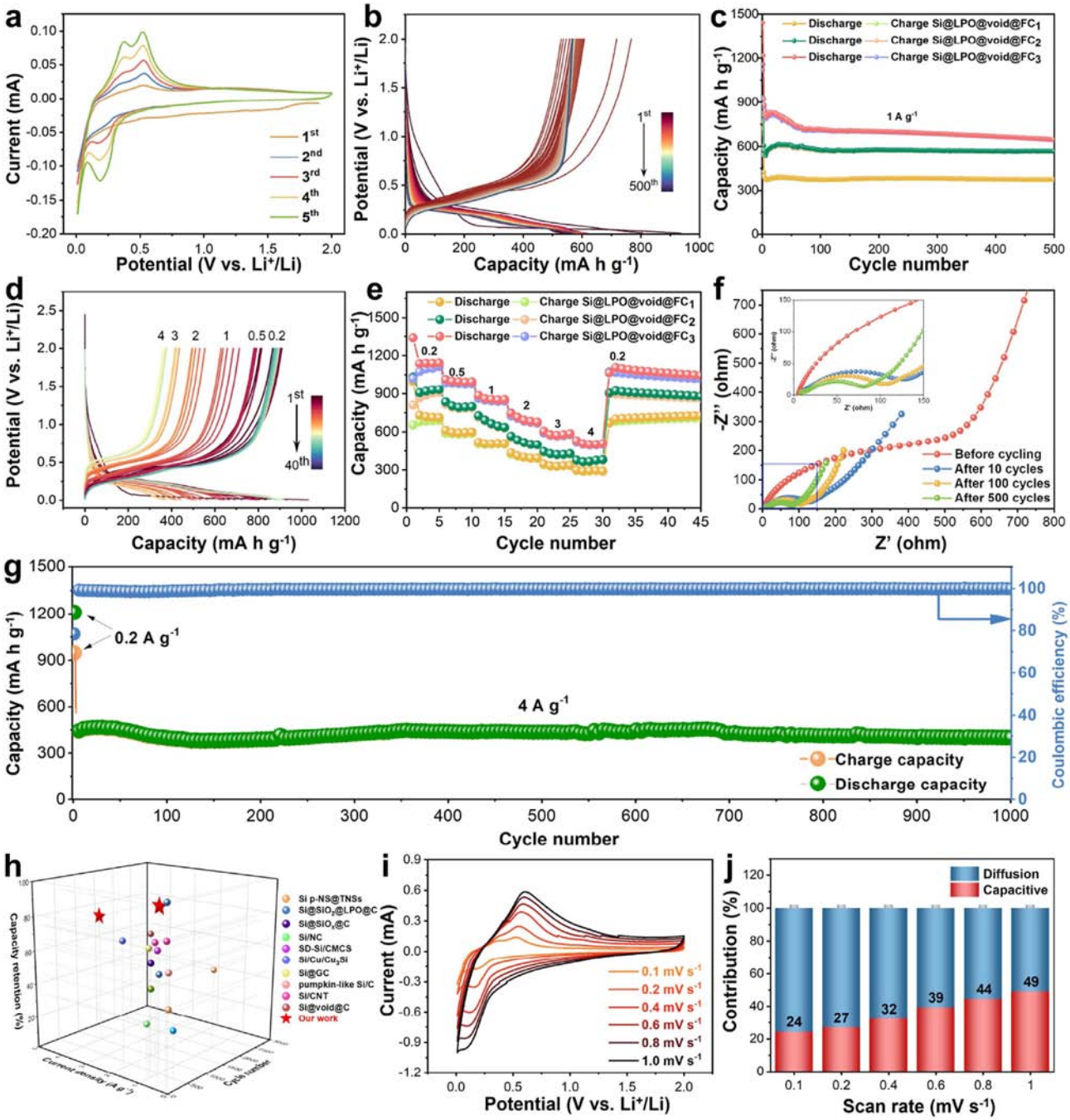

Fig. 3. Electrochemical properties in half cell. (a) CV curves of as-assembled half-cell at the scan rate of 0.1 mV/s. (b) Discharge-charge curves, (c) cycling performance of Si@LPO@void@FC anodes at 1 A/g. (d) Charge-discharge profiles at various current densities and (e) rate performance. (f) EIS of Si@LPO@void@FC_2 before and after different cycles at 4 A/g. (g) Long-term cycling performance of Si@LPO@void@FC_2 anode at 4 A/g. (h) Comparisons of the capacity retention of Si@LPO@void@FC_2 anodes with those of previously reported Si-based anodes [19,39–47]. (i) CV curves of Si@LPO@void@FC_2 with the increasing scan rates from 0.1 mV/s to 1.0 mV/s. (j) Capacitive contribution ratios in Si@LPO@void@FC_2 at different scan rates.

retention reaching 88% and 94% after 500 cycles, respectively. Fig. 3d presents the galvanic charge-discharge profiles of Si@LPO@void@FC_2 at different rates, apparently, a good rate capability can be obtained. Fig. 3e shows the comparisons of the rate performance of three Si@LPO@void@FC anodes. Obviously, the Si@LPO@void@FC_3 exhibits the highest capacity of 1180, 999, 861, 702, 584, 509 mAh/g as compared to Si@LPO@void@FC_1 (774, 599, 509, 406, 335, 294 mAh/g) and Si@LPO@void@FC_2 (944, 805, 673, 523, 428, 372 mAh/g) at various current densities of 0.2, 0.5, 1, 2, 3, 4 A/g. When the current density is reduced to 0.2 A/g, the Si@LPO@void@FC_1 and Si@LPO@void@FC_2 anodes show higher capacity recover as compared to Si@LPO@void@FC_3. In this regard, the achieved cycling performance and reversible capacity should be considered, and thus the Si@LPO@void@FC_2 with middle content of Si, is regarded as the most promising anode candidate. Additionally, in order to understand the role of F-doped carbon layer (denoted as bare FC), control experiment was conducted by directly pyrolyzing PTFE. Fig. S9 exhibits the morphology and composition of bare FC, and the EDS result shows that the bare FC is mainly composed of C, F and O. As for the electrochemical performance of bare FC

(Fig. S10), it shows extraordinary cycling stability with low specific capacity (184.9 mAh/g after 500 cycles at 1 A/g with 89% capacity retention and 119 mAh/g after 1000 cycles at 4 A/g with 85% capacity retention). However, benefiting from its high intrinsic electronic conductivity, bare FC exhibits superior rate performance. Thus, the capacity contribution of Si@LPO@void@FC is mainly originated from Si, and the coated F-doped carbon layer is beneficent to the fast reaction kinetics. Moreover, the improved kinetics of the Si@LPO@void@FC_2 is confirmed by the electrochemical impendance spectroscopy (EIS) tests (Fig. 3f and Fig. S11a). As compared to the bare Si anode (Fig. S11b), the Si@LPO@void@FC_2 exhibits lower charge-transfer resistance (fitted based on the equivalent circuit in Fig. S11c) before and after cycling, suggesting the importance role of LPO and FC coating that makes great contributions to the enhanced reaction kinetics.

The long-term cycling performance of three Si@LPO@void@FC anodes were evaluated, as shown in Fig. 3g and Figs. S12a–b. Due to the syngenetic effects of LPO layer and void-preserving FC, the Si@LPO@void@FC_2 anode can deliver a high specific capacity of 400 mAh/g even after 1000 cycles at high current density of 4 A/g with 76% capacity retention (Fig. 3g). This cycling performance is superior to several previously reported results of Si-based anodes as summarized in Fig. 3h and Table S2 [19,39–47]. In contrast, the Si@LPO@void@FC_1 and Si@LPO@void@FC_3 can deliver specific capacities of 342 and 425 mAh/g after 1000 cycles with 90% and 64% capacity retention, respectively (Figs. S12a–b).

In order to reveal the kinetic mechanism of Si@LPO@void@FC_2 anode, the CV curves at various scan rates were applied (Fig. 3i). The Li^+ storage mechanism of electrode can be analyzed according to the equation of $i = av^b$, where i and v represent the value of peak current and scan rate, respectively. When the b value is close to 0.5, indicating that the diffusion-controlled mechanism plays a dominated role. When the b value approaches 1.0, suggesting that the Li^+ storage mechanism of electrode can be attributed to a capacitive-controlled process. In present case, the b value can be determined as 0.61 (Fig. S13), demonstrating that the diffusion-controlled Li^+ storage mechanism is responsible for Si@LPO@void@FC_2 anode. Additionally, the capacitive contribution ratio at the high scan rate of 1 mV/s is still below 50% (Fig. 3j), further indicating that it belongs to a diffusion-dominated reaction process.

To demonstrate the structural stability during cycling, *in situ* TEM observations were conducted to visualize the live lithiation/delithiation process of Si@LPO@void@FC anode, and the schematic diagram of *in situ* TEM equipment is depicted in Fig. S14, as reported in previous works [48,49]. Once the Si@LPO@void@FC_2 electrode contacts with Li/Li_2O end, a biasing voltage (3 V/−3 V) can be applied to initiate the lithiation/delithiation process, as presented in the time-lapse TEM images (Fig. 4a–c) captured from Movie S1. The electrode undergoes volume expansion immediately upon lithiation, indicating that the LPO layer possess sufficient ionic transport pathways. After full lithiation, the diffraction spots of Si in pristine sample (Fig. 4e) cannot be detected, whereas new patterns of $Li_{22}Si_5$ phase are generated in the SAED patterns of lithiated Si@LPO@void@FC_2 (Fig. 4g), suggesting that the complete alloy reaction occurs between Si and Li^+. Meanwhile, the diffraction patterns of Li_3PO_4 and $Li_4P_2O_7$ can be still observed in the SAED patterns of lithiated sample, indicating that LPO is not involved in the reactions during the whole lithiation process. This phenomenon is consistent with the results of CV tests. Interestingly, the Si@LPO@void@FC_2 electrode remains its intrinsic structure well during the whole lithiation process with negligible mechanical damage. In contrast, during the delithiation process, the lithiated Si@LPO@void@FC_2 electrode is accordingly shrunk (Fig. 4d). It should be emphasized that the Si@LPO@void@FC_2 electrode can be expanded and shrunk reversibly without observable mechanical degradation in multiple lithiation/delithiation cycles (Fig. 4h–k), suggesting that the robust structure can be produced. Fig. 4f presents the dimension evolution of three particles (as marked in Fig. 4a). Even after five cycles, the active Si nanoparticles are expanded from 486, 279, 506 nm to 742, 367, 718 nm, respectively, with the average expansion ratio of 42% compared with initial 2D projected area. Note that the as-marked particles represent the aggregation of Si nanoparticles with LPO protection rather than the single Si nanoparticle, because the diameter of commercial Si particle is much smaller than that of the as-marked nanoparticles (Fig. S1). Fig. 4l-p and Movie S2 display the evolution of voids during lithiation/delithiation cycling. As shown in Fig. 4q, it can be found that the void is gradually filled to buffer the volume expansion during lithiation and can partly recover during delithiation. The above factors can be collectively beneficent for ameliorating the volume variations and reinforcing the structural stability during cycling, which are favorable for the enhanced long-term cycling stability. In contrast, as shown in Fig. S15a-d and Movie S3, the commercial Si NPs electrode is subjected to extremely large volume expansion, leading to fatal mechanical fracture. Although, the Si NPs are slightly shrunk during the delithiation process (Fig. S15e-h), the presence of cracking can be found in the bare Si nanoparticles electrode. This result clearly indicates that bare Si without surface coating suffers from significant volume change with remarkable mechanical degradation, eventually leading to fast capacity decay.

Supplementary data related to this article can be found at https://doi.org/10.1016/j.mtnano.2023.100322.

To further disclose the structural evolution of Si@LPO@void@FC_2 and bare Si nanoparticles anodes after long-term cycling, both the *ex situ* TEM and SEM observations were conducted. Fig. 5a and c exhibit the SEM images of Si@LPO@void@FC_2 and bare Si electrode before cycling, respectively. Both the Si@LPO@void@FC_2 and Si anodes show similar morphologies without observable cracking at low magnification. However, the apparent cracking begins to form only after 10 cycles at the current density of 4 A/g (Fig. S16b) for bare Si anode, and it becomes larger with the prolonged cycling (Fig. S16d and Fig. 5d). Impressively, no observable mechanical damage such as cracking can be found in Si@LPO@void@FC_2 electrode after 100 cycles (Fig. S16a and b). Even after 500 cycles, only slight cracking can be observed (Fig. 5b). Furthermore, the Si NPs can be easily identified by the STEM observation and its corresponding EDS mappings of cycled Si@LPO@void@FC_2 electrode (Fig. 5e–j). And, the signals of P, C, O and F elements uniformly distributed around Si NPs (Fig. 5g–j), confirming the structural stability can be achieved. Fig. 5k presents the EDS results of cycled Si@LPO@void@FC_2 anode. It demonstrates that the contents of P and F are higher than those of pristine sample, which are probably originated from the electrolyte and SEI layer. For SAED patterns of cycled Si@LPO@void@FC_2 (Fig. S17), the diffraction spots of Si, Li_3PO_4 and $Li_4P_2O_7$ can be detected as well, elucidating that the LPO layer still plays an important role in preventing Si from being fractured after long-term cycling. In contract, without the protection of LPO, isolative Si NPs cannot be easily distinguished after 500 cycles (Fig. S18), which is ascribed to the mechanical damage and continued reaction between electrolyte with Si. These results clearly reveal that the dual shell of LPO and void-preserving FC on Si can bring about significant benefits for accommodating the large volume changes of Si while ensuring stable SEI, giving rise to superior long-term cycling stability. Based on the experimental results as discussed above, the schematic diagram of structural evolution for commercial Si anodes and Si@LPO@void@FC_2 are illustrated in Fig. 5l, suggesting that the advantageously structural design is favorable for achieving the stable Si anode.

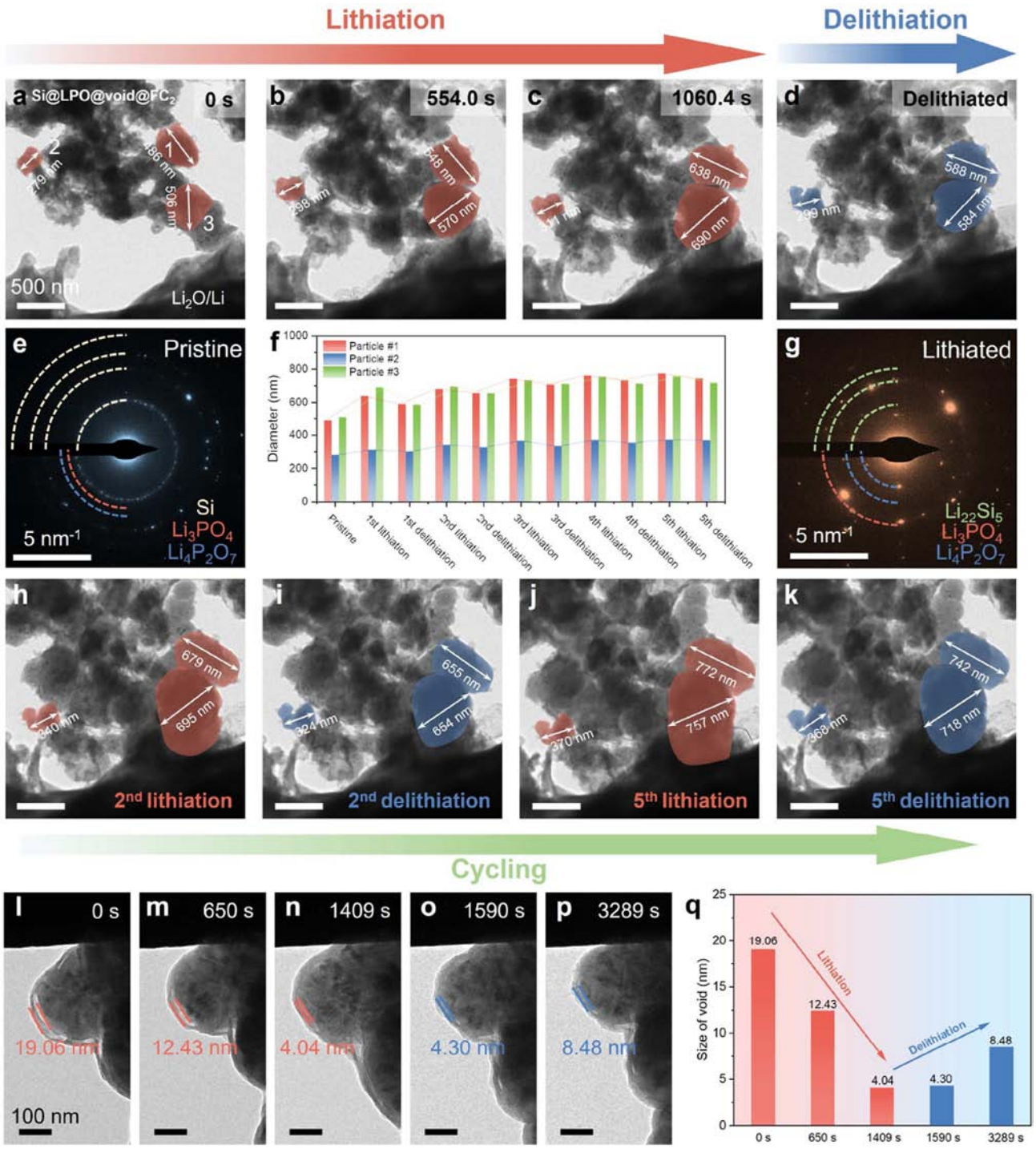

Fig. 4. *In situ* TEM characterization of Si@LPO@void@FC_2 anodes. (a–d) Time-lapsed TEM images of the initial cycle process for Si@LPO@void@FC_2 anode. SAED patterns (e) before and (g) after lithiation. (f) The dimension changes of three particles (marked particles in TEM image). (h–k) The morphology evolution of Si@LPO@void@FC_2 anode during the second and fifth cycles. Void evolution during (l–n) lithiation process and (o, p) delithiation process. (q) Histogram of the dimension evolution of void during cycling.

In order to evaluate the feasibility for practical application, a full LIB cell consisting of Si@LPO@void@FC_2 anode and commercial $LiFePO_4$ cathode is assembled as shown in Fig. 6a. This full cell can easily light up the 32 XMU (Xiamen University) logo of the red LED array (Fig. 6b). Besides, it exhibits a superior cycling stability, delivering a high reversible capacity of 117 mAh/g with 92% capacity retention after 150 cycles at 1 C (Fig. 6c and d), outperforming several reported full cells assembled with Si-based anodes (Fig. 6e) and holding promise for practical applications.

3. Conclusions

In summary, we have proposed the successful design and synthesis a core– dual shell structured Si@L_3PO_4/$Li_4P_2O_7$@void@FC multicomponent anode for boosting the LIB performance. The core of Si NP ensures high-capacity, while the interior mechanical robust L_3PO_4/$Li_4P_2O_7$ shell and exterior void-preserving F-doped C shell can bring about significant benefits for accommodating volume changes, upgrading the Li^+/e^- transport kinetics and reinforcing

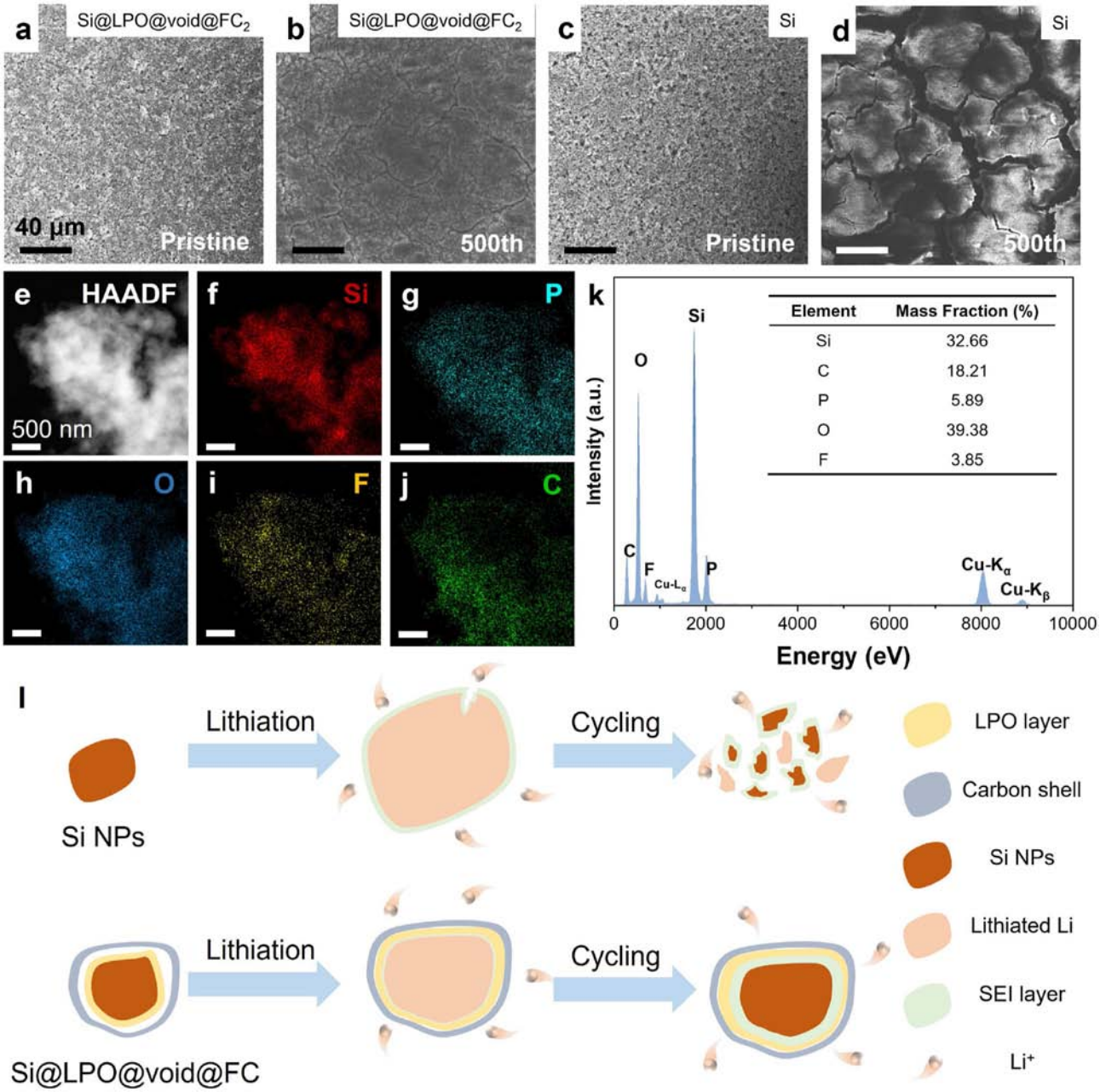

Fig. 5. Morphologies and compositions of Si@LPO@void@FC_2 anodes after cycling. SEM images of (a) pristine, (b) cycled Si@LPO@void@FC_2, (c) pristine, (d) cycled commercial Si anode. (e–j) HAADF image and corresponding elemental mappings of Si@LPO@void@FC_2 anode after 500 cycles. (k) EDS analysis of cycled Si@LPO@void@FC_2 anode and the corresponding elemental mass fraction. (l) Schematic diagram of the structural evolution of commercial Si and Si@LPO@void@FC_2 anodes during cycling.

structural stability. Using *in situ/ex situ* TEM observations with the combination of *ex situ* SEM observations, it reveals that the volume expansion of Si NPs can be effectively accommodated by beneficial effects form void-preserving F-doped C and LPO layer. Besides, the overall electrode structure of Si@LPO@void@FC is sufficiently robust without observable mechanical degradation during cycling, which makes great contributions to long-term cycling stability. Accordingly, the as-obtained Si@LPO@void@FC_2 anode delivers a high reversible capacity of 569 mAh/g at 1 A/g after 500 cycles, and a superior long-term stability over 1000 cycles at high current density of 4 A/g with 76% capacity retention can be achieved. Impressively, when paired with a commercial $LiFePO_4$ cathode, the full cell also displays the favorable cycling stability (117 mAh/g, 1C for over 150 cycles with 92% capacity retention). As excepted, this work can provide insights into the development of stable Si-based composite anodes by taking the advantage of artificial SEI design and void-preserving carbon modification strategy. It also offers the opportunities for the design of other electrode materials that normally undergo large volume change with enhanced performance.

4. Experimental section

4.1. Synthesis of Si@LPO@void@FC and bare FC was purchased

In a typical synthesis process, 33 mg CH_3COOLi was dissolved in DI water. Then a certain amount of commercial Si NPs (with the

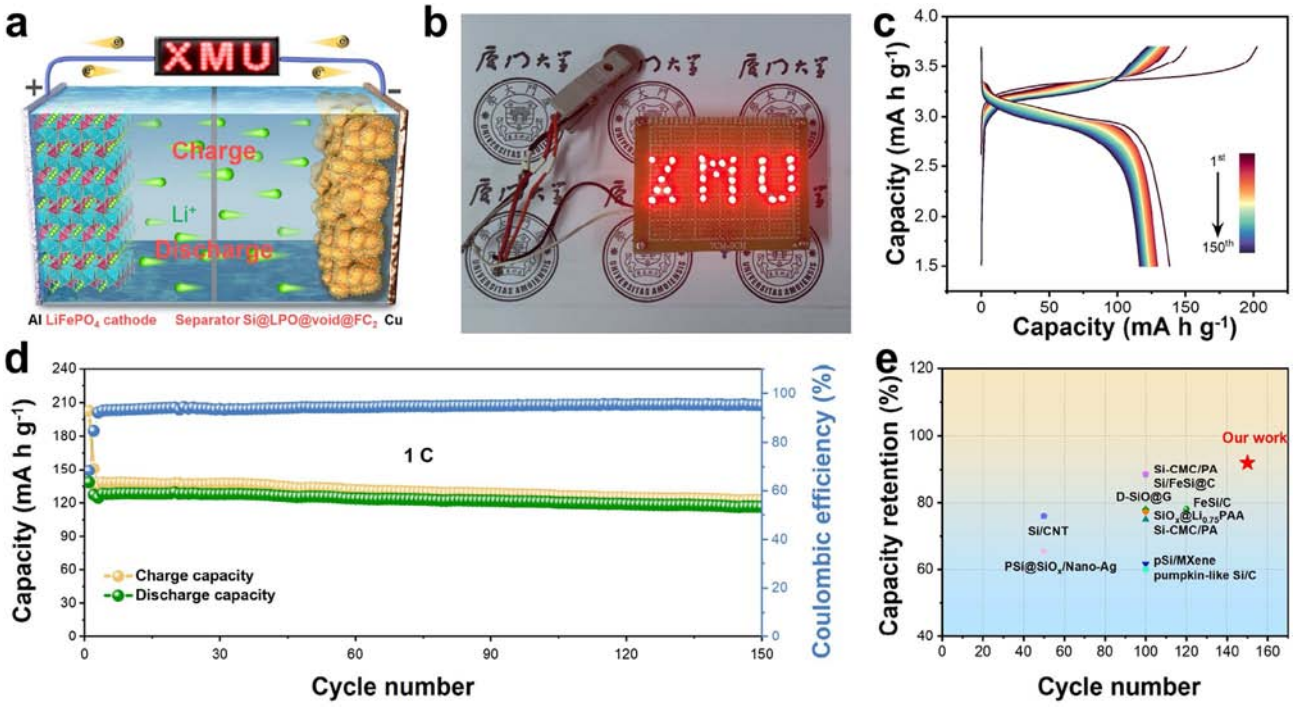

Fig. 6. (a) Schematic illustration of the full cell. (b) Photograph of the "XMU" logo consists of LEDs lighted up by as-assembled full cell. (c) Charge-discharge profiles and (d) cycling performance of full cell at 1C. (e) Capacity retention comparison between this work with other full cells assembled with Si-based anode materials [33,45,46,50–56].

contents of 45 mg, 60 mg and 90 mg, which was purchased from Zhejiang Zhongning Silicon Industry Co., Ltd., were added in the solution dispersed with the assistance of ultrasonic, respectively. Subsequently, 50 μL PA and 50 μL PTFE solution were added under magnetic stirring for 10 min, respectively. After then, the as-obtained solution was frozen by liquid nitrogen and dried by lyophilization. Finally, the dried powders were transferred to tubular furnace and sintered at 600 °C for 2 h under the protection of Ar atmosphere. The bare FC was fabricated by directly pyrolyzing the PTFE precursor under the protection of argon at 600 °C.

4.2. Materials characterization

The morphologies and structures of as-prepared samples were characterized by scanning electron microscopy (Zeiss SIGMA) and transmission electron microscopy (FEI Talos F200s). The X-ray diffraction patterns were obtained by Bruker-axs XRD (Cu $K_{\alpha 1}$ source, $\lambda = 1.5418$ Å). The chemical compositions of the samples were analyzed by X-ray photoelectron energy spectra (XPS, Thermo Fisher, Thermo Scientific K-Alpha+). The TGA was conducted on a Netzsch STA 2500 under air condition with the heating rate of 10 °C/min.

4.3. Electrochemical test

In order to prepare the working electrodes, the active material, Super P and carboxymethyl cellulose (CMC) were mixed with the mass ratio of 8:1:1. After added a certain amount of DI water, such mixture was milled for 8 h to form a homogeneous slurry. Subsequently, the slurry was coated on the copper foil and cut into electrode discs with the diameter of 12 mm. The mass loading of the Si@LPO@void@FC is controlled at the range of 0.8–1.2 mg/cm^2 on each of disks. The specific capacity of anode is calculated based on the whole mass of Si@LPO@void@FC. After then, the electrode disk was assembled into CR2025 coin-cells using Li metal foil as counter electrode and Celgard 2400 film as separator. 1 M $LiPF_6$ in a mixture of ethylene carbonate, diethyl carbonate and dimethyl carbonate (1:1:1) was selected as electrolyte. The electrochemical tests were carried out on Neware battery test system with a voltage range of 0.01–2 V at room temperature. CV tests and EIS were conducted on an electrochemical workstation (CHI 660E, Chenhua, Shanghai). For EIS measurement, a voltage amplitude of 10 mV was applied in the frequency range of 10 MHz to 0.01 Hz. For the full cell battery tests, the prelithiated Si@LPO@void@FC_2 and commercial $LiFePO_4$ (LFP) were applied as anode and cathode, respectively. The prelithiation process for Si@LPO@void@FC_2 anode was conducted using half cells by discharging to 0.01 V at 0.2 A/g, considering the relatively low ICE of about 82%. The cathode disks were fabricated by mixing commercial LFP, Super P and PVDF with the mass ratio of 8:1:1 in N-methyl-2-pyrrolidone to form a uniform slurry. The electrochemical tests were conducted on Neware battery test system at a voltage range of 1.5–3.7 V. Besides, in order to balance the capacity between cathode and anode, the mass of active materials in anode was slightly excessive to the cathode side and the N/P ratio was controlled to be 1.2:1. The capacity of full cell is calculated based on the mass of active materials in cathode.

4.4. In situ TEM observation

The dynamic lithiation process of Si@LPO@void@FC and Si NPs were observed by FEI Talos-F200s with a Nanofactory TEM-STM holder. The Si@LPO@void@FC_2 or Si NPs was placed on a Mo tip as the working electrode and Li metal with naturally formed Li_2O was placed on a Cu tip. The naturally formed Li_2O layer serve as electrolyte. Once the Li/Li_2O contact the working electrode, a positive biasing voltage (3 V) was applied on the Cu tip to initiate the lithiation process. By reversing the applied voltage (−3 V), the delithiation process can be observed. Moreover, to minimize the

influence of electron beam, the electron beam dosage was controlled below 1 A/cm^2.

Credit author statement

Zhefei Sun: Data curation, Writing- Original draft preparation; Miao Li: Data curation, Writing- Original draft preparation; Zhiming Zheng: Data curation, Reviewing and Editing; Zhilin Chen: Data curation, Reviewing and Editing; Hehe Zhang: Data curation, Editing; Bensheng Xiao: Editing; Baihua Qu: Reviewing and Editing; Bing Jiang: Reviewing and Editing; Honggang Liao: Reviewing and Editing; Li Zhang: Reviewing and Editing; Meicheng Li: Reviewing and Editing; Qiaobao Zhang: Conceptualization, Supervision, Writing-Reviewing and Editing; Ming-Sheng Wang: Supervision, Reviewing and Editing

Declaration of competing interest

The authors declare that they have no known competing financial interests or personal relationships that could have appeared to influence the work reported in this paper.

Data availability

Data will be made available on request.

Acknowledgments

This work was financially supported by the National Natural Science Foundation of China (Grants Nos. 52072323, 52122211), the "Double First Class" Foundation of Materials and Intelligent Manufacturing Discipline of Xiamen University, and the State Key Laboratory of Alternate Electrical Power System with Renewable Energy Sources (Grant No. LAPS22005).

Appendix A. Supplementary data

Supplementary data to this article can be found online at https://doi.org/10.1016/j.mtnano.2023.100322.

References

[1] L. Qing, H. Yunhuan, Y. Xinrun, Q. Yufei, M. Tao, H. Xianluo, The pursuit of commercial silicon-based microparticle anodes for advanced lithium-ion batteries: a review, Nano Res. Energy 1 (2022), e9120037.
[2] K. Feng, M. Li, W. Liu, A.G. Kashkooli, X. Xiao, M. Cai, Z. Chen, Silicon-based anodes for lithium-ion batteries: from fundamentals to practical applications, Small 14 (2018), 1702737.
[3] M. Ko, S. Chae, J. Cho, Challenges in accommodating volume change of Si anodes for Li-ion batteries, Chemelectrochem 2 (2015) 1645–1651.
[4] X.H. Liu, L. Zhong, S. Huang, S.X. Mao, T. Zhu, J.Y. Huang, Size-dependent fracture of silicon nanoparticles during lithiation, ACS Nano 6 (2012) 1522–1531.
[5] Y. He, L. Jiang, T. Chen, Y. Xu, H. Jia, R. Yi, D. Xue, M. Song, A. Genc, C. Bouchet-Marquis, L. Pullan, T. Tessner, J. Yoo, X. Li, J.-G. Zhang, S. Zhang, C. Wang, Progressive growth of the solid–electrolyte interphase towards the Si anode interior causes capacity fading, Nat. Nanotechnol. 16 (2021) 1113–1120.
[6] D.H.S. Tan, Y.-T. Chen, H. Yang, W. Bao, B. Sreenarayanan, J.-M. Doux, W. Li, B. Lu, S.-Y. Ham, B. Sayahpour, J. Scharf, E.A. Wu, G. Deysher, H.E. Han, H.J. Hah, H. Jeong, J.B. Lee, Z. Chen, Y.S. Meng, Carbon-free high-loading silicon anodes enabled by sulfide solid electrolytes, Science 373 (2021) 1494–1499.
[7] M. Ge, C. Cao, G.M. Biesold, C.D. Sewell, S.-M. Hao, J. Huang, W. Zhang, Y. Lai, Z. Lin, Recent advances in silicon-based electrodes: from fundamental research toward practical applications, Adv. Mater. 33 (2021), 2004577.
[8] Y. Jin, B. Zhu, Z. Lu, N. Liu, J. Zhu, Challenges and recent progress in the development of Si anodes for lithium-ion battery, Adv. Energy Mater. 7 (2017), 1700715.
[9] N. Liu, Z. Lu, J. Zhao, M.T. McDowell, H.-W. Lee, W. Zhao, Y. Cui, A pomegranate-inspired nanoscale design for large-volume-change lithium battery anodes, Nat. Nanotechnol. 9 (2014) 187–192.
[10] Z. Zheng, H.-H. Wu, H. Chen, Y. Cheng, Q. Zhang, Q. Xie, L. Wang, K. Zhang, M.-S. Wang, D.-L. Peng, Fabrication and understanding of Cu_3Si-Si@ carbon@ graphene nanocomposites as high-performance anodes for lithium-ion batteries, Nanoscale 10 (2018) 22203–22214.
[11] C.-Z. Ke, F. Liu, Z.-M. Zheng, H.-H. Zhang, M.-T. Cai, M. Li, Q.-Z. Yan, H.-X. Chen, Q.-B. Zhang, Boosting lithium storage performance of Si nanoparticles via thin carbon and nitrogen/phosphorus co-doped two-dimensional carbon sheet dual encapsulation, Rare Met. 40 (2021) 1347–1356.
[12] F. Luo, B. Liu, J. Zheng, G. Chu, K. Zhong, H. Li, X. Huang, L. Chen, Review—nano-silicon/carbon composite anode materials towards practical application for next generation Li-ion batteries, J. Electrochem. Soc. 162 (2015) A2509.
[13] T. Jaumann, J. Balach, U. Langklotz, V. Sauchuk, M. Fritsch, A. Michaelis, V. Teltevskij, D. Mikhailova, S. Oswald, M. Klose, G. Stephani, R. Hauser, J. Eckert, L. Giebeler, Lifetime vs. rate capability: understanding the role of FEC and VC in high-energy Li-ion batteries with nano-silicon anodes, Energy Storage Mater. 6 (2017) 26–35.
[14] Y. Jin, S. Li, A. Kushima, X. Zheng, Y. Sun, J. Xie, J. Sun, W. Xue, G. Zhou, J. Wu, Self-healing SEI enables full-cell cycling of a silicon-majority anode with a coulombic efficiency exceeding 99.9, Energy Environ. Sci. 10 (2017) 580–592.
[15] Q. Ai, D. Li, J. Guo, G. Hou, Q. Sun, Q. Sun, X. Xu, W. Zhai, L. Zhang, J. Feng, P. Si, J. Lou, L. Ci, Artificial solid electrolyte interphase coating to reduce lithium trapping in silicon anode for high performance lithium-ion batteries, Adv. Mater. Interfaces 6 (2019), 1901187.
[16] Q. Ai, Q. Fang, J. Liang, X. Xu, T. Zhai, G. Gao, H. Guo, G. Han, L. Ci, J. Lou, Lithium-conducting covalent-organic-frameworks as artificial solid-electrolyte-interphase on silicon anode for high performance lithium ion batteries, Nano Energy 72 (2020), 104657.
[17] N. Kuwata, N. Iwagami, Y. Matsuda, Y. Tanji, J. Kawamura, Thin film batteries with Li_3PO_4 solid electrolyte fabricated by pulsed laser deposition, ECS Trans. 16 (2009) 53.
[18] T. Deng, X. Ji, Y. Zhao, L. Cao, S. Li, S. Hwang, C. Luo, P. Wang, H. Jia, X. Fan, X. Lu, D. Su, X. Sun, C. Wang, J.G. Zhang, Tuning the anode–electrolyte interface chemistry for garnet-based solid-state Li metal batteries, Adv. Mater. 32 (2020), 2000030.
[19] L. Gu, J. Han, M. Chen, W. Zhou, X. Wang, M. Xu, H. Lin, H. Liu, H. Chen, J. Chen, Q. Zhang, X. Han, Enabling robust structural and interfacial stability of micron-Si anode toward high-performance liquid and solid-state lithium-ion batteries, Energy Storage Mater. 52 (2022) 547–561.
[20] H. Zhang, J. Luo, M. Qi, S. Lin, Q. Dong, H. Li, N. Dulock, C. Povinelli, N. Wong, W. Fan, J.L. Bao, D. Wang, Enabling lithium metal anode in nonflammable phosphate electrolyte with electrochemically induced chemical reactions, Angew. Chem. Int. Ed. 60 (2021) 19183–19190.
[21] H. Jiang, J. Liu, M. Wang, J. Wang, T. Sun, L. Hu, J. Zhu, Y. Tang, J. Wang, Stable rooted solid electrolyte interphase for lithium-ion batteries, J. Phys. Chem. Lett. 12 (2021) 10521–10531.
[22] E. Kartini, V. Yapriadi, H. Jodi, M. Manawan, C. Panghegar, Wahyudianingsih, Solid electrolyte composite $Li_4P_2O_7$–Li_3PO_4 for lithium ion battery, Prog. Nat. Sci. Mater. Int. 30 (2020) 168–173.
[23] W. An, B. Gao, S. Mei, B. Xiang, J. Fu, L. Wang, Q. Zhang, P.K. Chu, K. Huo, Scalable synthesis of ant-nest-like bulk porous silicon for high-performance lithium-ion battery anodes, Nat. Commun. 10 (2019) 1447.
[24] W. An, P. He, Z. Che, C. Xiao, E. Guo, C. Pang, X. He, J. Ren, G. Yuan, N. Du, D. Yang, D.-L. Peng, Q. Zhang, Scalable synthesis of pore-rich Si/C@C core–-shell-structured microspheres for practical long-life lithium-ion battery anodes, ACS Appl. Mater. Interfaces 14 (2022) 10308–10318.
[25] Y.S. Lee, Y.K. Sun, K.S. Nahm, Synthesis and characterization of $LiNiO_2$ cathode material prepared by an adiphic acid-assisted sol–gel method for lithium secondary batteries, Solid State Ion. 118 (1999) 159–168.
[26] A.N. García, N. Viciano, R. Font, Products obtained in the fuel-rich combustion of PTFE at high temperature, J. Anal. Appl. Pyrolysis 80 (2007) 85–91.
[27] A.L.M. Daneluti, J.d.R. Matos, Study of thermal behavior of phytic acid, Brazil. J. Pharmaceut. Sci. 49 (2013) 275–283.
[28] T. Kyotani, Control of pore structure in carbon, Carbon 38 (2000) 269–286.
[29] H. Mi, X. Yang, Y. Li, P. Zhang, L. Sun, A self-sacrifice template strategy to fabricate yolk-shell structured silicon@void@carbon composites for high-performance lithium-ion batteries, Chem. Eng. J. 351 (2018) 103–109.
[30] N.-W. Li, Y.-X. Yin, C.-P. Yang, Y.-G. Guo, An artificial solid electrolyte interphase layer for stable lithium metal anodes, Adv. Mater. 28 (2016) 1853–1858.
[31] K. Hu, X. Qi, C. Lu, K. Du, Z. Peng, Y. Cao, G. Hu, Enhanced electrochemical performance of $LiNi_{0.8}Co_{0.1}Mn_{0.1}O_2$ cathode materials via $Li_4P_2O_7$ surface modification for Li-ion batteries, Ceram. Int. 44 (2018) 14209–14216.
[32] Y. Ruan, Y. Lu, X. Huang, J. Su, C. Sun, J. Jin, Z. Wen, Acid induced conversion towards a robust and lithiophilic interface for Li–$Li_7La_3Zr_2O_{12}$ solid-state batteries, J. Mater. Chem. 7 (2019) 14565–14574.
[33] Z. Zheng, H. Gao, C. Ke, M. Li, Y. Cheng, D.-L. Peng, Q. Zhang, M.-S. Wang, Constructing robust cross-linked binder networks for silicon anodes with improved lithium storage performance, ACS Appl. Mater. Interfaces 13 (2021) 53818–53828.
[34] B.H. Shen, S. Wang, W.E. Tenhaeff, Ultrathin conformal polycyclosiloxane films to improve silicon cycling stability, Sci. Adv. 5 (2019), eaaw4856.
[35] Y. Liu, Q. Li, X. Guo, X. Kong, J. Ke, M. Chi, Q. Li, Z. Geng, J. Zeng, A highly efficient metal-free electrocatalyst of F-doped porous carbon toward N_2 electroreduction, Adv. Mater. 32 (2020), 1907690.

[36] J. Hu, L. Zhang, Achieving F-doped porous hollow carbon nanospheres with ultrahigh pore volume via a gas–solid interface reaction, J. Mater. Chem. 9 (2021) 27560–27567.
[37] J. Xie, X. Zhao, M. Wu, Q. Li, Y. Wang, J. Yao, Metal-Free fluorine-doped carbon electrocatalyst for CO_2 reduction outcompeting hydrogen evolution, Angew. Chem. Int. Ed. 57 (2018) 9640–9644.
[38] Q. Zhang, H. Chen, L. Luo, B. Zhao, H. Luo, X. Han, J. Wang, C. Wang, Y. Yang, T. Zhu, M. Liu, Harnessing the concurrent reaction dynamics in active Si and Ge to achieve high performance lithium-ion batteries, Energy Environ. Sci. 11 (2018) 669–681.
[39] M. Xia, B. Chen, F. Gu, L. Zu, M. Xu, Y. Feng, Z. Wang, H. Zhang, C. Zhang, J. Yang, $Ti_3C_2T_x$ MXene nanosheets as a robust and conductive tight on Si anodes significantly enhance electrochemical lithium storage performance, ACS Nano 14 (2020) 5111–5120.
[40] R.F.H. Hernandha, P.C. Rath, B. Umesh, J. Patra, C.-Y. Huang, W.-W. Wu, Q.-F. Dong, J. Li, J.-K. Chang, Supercritical CO_2-assisted SiO_x/carbon multi-layer coating on Si anode for lithium-ion batteries, Adv. Funct. Mater. 31 (2021), 2104135.
[41] Y. Ma, A. Huang, Y. Li, H. Jiang, W. Zhang, L. Zhang, L. Li, S. Peng, Simple preparation of Si/N-doped carbon anodes from photovoltaic industry waste for lithium-ion batteries, J. Alloys Compd. 890 (2022), 161792.
[42] Y. Hu, Y. Qiao, Z. Xie, L. Li, M. Qu, W. Liu, G. Peng, Water-soluble polymer assists multisize three-dimensional microspheres as a high-performance Si anode for lithium-ion batteries, ACS Appl. Energy Mater. 4 (2021) 9673–9681.
[43] S. Suh, H. Yoon, H. Park, J. Kim, H.-J. Kim, Enhancing the electrochemical performance of silicon anodes for lithium-ion batteries: one-pot solid-state synthesis of Si/Cu/Cu_3Si/C electrode, Appl. Surf. Sci. 567 (2021), 150868.
[44] R. Shao, J. Niu, F. Zhu, M. Dou, Z. Zhang, F. Wang, A facile and versatile strategy towards high-performance Si anodes for Li-ion capacitors: concomitant conductive network construction and dual-interfacial engineering, Nano Energy 63 (2019), 103824.
[45] Y. Zeng, Y. Huang, N. Liu, X. Wang, Y. Zhang, Y. Guo, H.-H. Wu, H. Chen, X. Tang, Q. Zhang, N-doped porous carbon nanofibers sheathed pumpkin-like Si/C composites as free-standing anodes for lithium-ion batteries, J. Energy Chem. 54 (2021) 727–735.
[46] Z. Yi, N. Lin, Y. Zhao, W. Wang, Y. Qian, Y. Zhu, Y. Qian, A flexible micro/nanostructured Si microsphere cross-linked by highly-elastic carbon nanotubes toward enhanced lithium ion battery anodes, Energy Storage Mater. 17 (2019) 93–100.
[47] F. Wang, B. Wang, T. Ruan, T. Gao, R. Song, F. Jin, Y. Zhou, D. Wang, H. Liu, S. Dou, Construction of structure-tunable Si@void@C anode materials for lithium-ion batteries through controlling the growth kinetics of resin, ACS Nano 13 (2019) 12219–12229.
[48] L. Chao, L. Bowen, J. Ningyi, D. Yi, Elucidating the charge-transfer and Li-ion-migration mechanisms in commercial lithium-ion batteries with advanced electron microscopy, Nano Res. Energy 1 (2022), e9120031.
[49] Z. Sun, M. Li, B. Xiao, X. Liu, H. Lin, B. Jiang, H. Liu, M. Li, D.-L. Peng, Q. Zhang, In situ transmission electron microscopy for understanding materials and interfaces challenges in all-solid-state lithium batteries, eTransportation (2022), 100203.
[50] Z. Zhang, H. Ying, P. Huang, S. Zhang, Z. Zhang, T. Yang, W.-Q. Han, Porous Si decorated on MXene as free-standing anodes for lithium-ion batteries with enhanced diffusion properties and mechanical stability, Chem. Eng. J. 451 (2023), 138785.
[51] S. Xu, J. Zhou, J. Wang, S. Pathiranage, N. Oncel, P. Robert Ilango, X. Zhang, M. Mann, X. Hou, In situ synthesis of graphene-coated silicon monoxide anodes from coal-derived humic acid for high-performance lithium-ion batteries, Adv. Funct. Mater. 31 (2021), 2101645.
[52] L. Hu, M. Jin, Z. Zhang, H. Chen, F. Boorboor Ajdari, J. Song, Interface-adaptive binder enabled by supramolecular interactions for high-capacity Si/C composite anodes in lithium-ion batteries, Adv. Funct. Mater. 32 (2022), 2111560.
[53] F. Xi, Z. Zhang, Y. Hu, S. Li, W. Ma, X. Chen, X. Wan, C. Chong, B. Luo, L. Wang, PSi@SiO_x/Nano-Ag composite derived from silicon cutting waste as high-performance anode material for Li-ion batteries, J. Hazard Mater. 414 (2021), 125480.
[54] Q. Ma, Y. Zhao, Z. Hu, J. Qu, Z. Zhao, H. Xie, P. Xing, D. Wang, H. Yin, Electrochemically converting micro-sized industrial Si/$FeSi_2$ to nano Si/FeSi for the high-performance lithium-ion battery anode, Mater, Today Energy 21 (2021), 100817.
[55] Z. Li, W. Tang, Y. Yang, G. Lai, Z. Lin, H. Xiao, J. Qiu, X. Wei, S. Wu, Z. Lin, Engineering prelithiation of polyacrylic acid binder: a universal strategy to boost initial coulombic efficiency for high-areal-capacity Si-based anodes, Adv. Funct. Mater. 32 (2022), 2206615.
[56] H. Wang, M. Miao, H. Li, Y. Cao, H. Yang, X. Ai, In situ-formed artificial solid electrolyte interphase for boosting the cycle stability of Si-based anodes for Li-ion batteries, ACS Appl. Mater. Interfaces 13 (2021) 22505–22513.